ELSEVIER

Volume 183, Issue 10, October 2010

JOURNAL OF SOLID STATE CHEMISTRY

www.elsevier.com/locate/jssc

CONTENTS

Abstracted/indexed in BioEngineering Abstracts, Chemical Abstracts, Coal Abstracts, Current Contents/Physics, Chemical, & Earth Sciences, Engineering Index, Research Alert, SCISEARCH, Science Abstracts, and Science Citation Index. Also covered in the abstract and citation database SCOPUS®. Full text available on ScienceDirect®.

Regular Articles

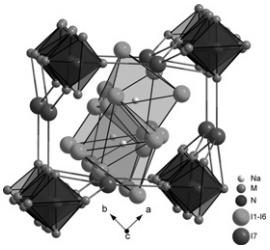

View at the main structural features of the $NaM_4N_2I_7$ series (M = La–Nd): The $^{1}_{\infty}\{[NM^{e}_{4/2}]^{3+}\}$ chains, consisting of *trans*-edge connected $[NM_4]^{9+}$ tetrahedra, and the special kind of iodide anions, namely $(I7)^{-}$, form cages, in which isolated $[NaI_6]^{5-}$ octahedra are embedded.

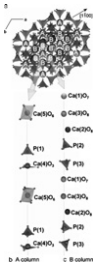

One of the 6*a* cation sites of the β- $Ca_3(PO_4)_2$ structure has previously been described as half occupied. Here, classical static lattice techniques are used to model the different configurations that the Ca ions can exhibit over these Ca(4) 6*a* sites. All possible configurations in the single primitive unit cell and a hexagonal supercell ($3_h \times 1 \times 1$) have been generated, along with configurationally averaged structures, that exhibits experimentally reported $R\,3c$ symmetry. The lowest energy configuration of the primitive cell exhibits $R\,3$ symmetry. Conversely, the lowest energy configurations derived from the hexagonal supercell cell, which are considerably more stable, exhibit $P\,3_1$ and $P\,3_2$ symmetries, which are isomorphic supergroups of $R\,3c$. The implication of these simulations are discussed in terms of refined structural models of the material.

Regular Articles—Continued

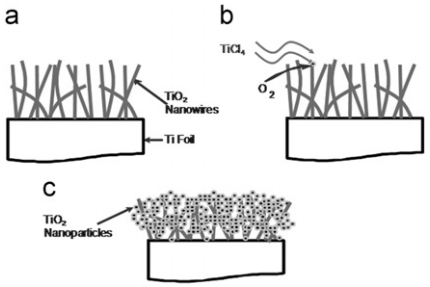

Schematic of proposed reaction mechanisms for synthesizing the hetero-structures: (a) TiO_2 nanowires were grown as base structures for capturing $TiCl_4$ gas. (b) $TiCl_4$ gas was oxidized, precipitating crystalline TiO_2 nanoparticles. (c) Repeated particle-incorporation process created tree-like hetero-structures.

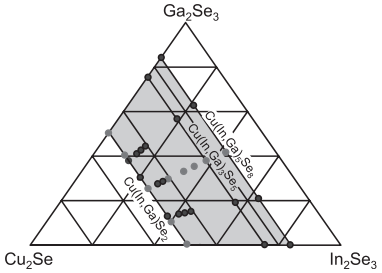

Pseudo-ternary diagram in the Cu_2Se–In_2Se_3–Ga_2Se_3 system showing the composition of all the synthesized compounds. The crystal structure of the compounds corresponding to red circles are presented in this study.

Continued

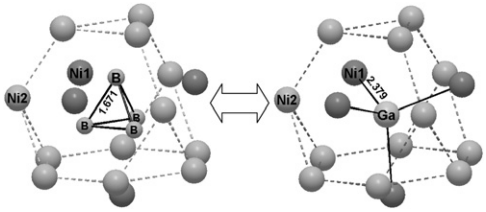

Crystal structure of τ-Borides $M_{23}B_6$; $M1$: M_8-cubes, $M2$: M_{12}-cuboctahedra centred by $M3$, isolated M-atoms: $M4$; grey circles: boron, black circles: metal atoms.

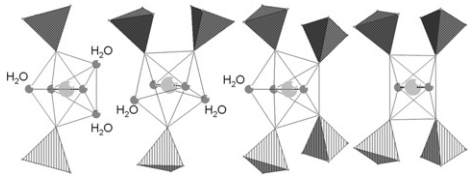

The various type of PBP pillars P2, P3, P4, and P4′ in the three-dimensional inorganic frameworks based on the uranophane-type sheet in monoamine templated uranyl-vanadates.

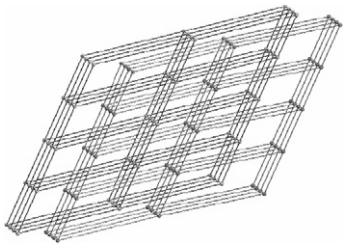

Two inorganic–organic 3D network, namely $\{[Ln(L)_{1.5}(H_2O)_2]\cdot 5H_2O\}n$ [Ln = Y (1), Ce (2)], have been prepared under hydrothermal condition and structurally characterized by single-crystal X-ray diffractions. Both **1** and **2** exhibit 3D network structures with 2-fold interpenetration. Interestingly, the reversible desorption–adsorption behavior of lattice water is significantly observed in the two compounds. The result shows their potential application as late-model water absorbent in the field of adsorption material.

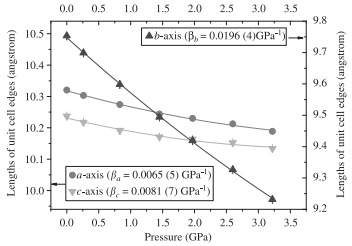

High pressure study of a synthetic gismondine zeolite reveals channel-dependent anisotropic compression, i.e., the b-axis, normal to the 8-ring channels, is three times more compressible than the a- and c-axes.

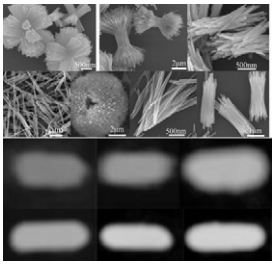

La(1,3,5-BTC)$(H_2O)_6$ with 3D flowerlike, wheatearlike, spherical, sheaflike, taillike, bundlelike architectures, and 1D nanorods were selectively prepared; color-tunable photoluminescence from red to green was also realized by co-doping Eu^{3+} and Tb^{3+}.

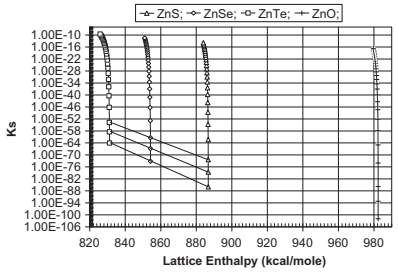

For the Zn-chalcogenides, the quantities n and I_e are 2.007 and 650.3 kcal (2722 kJ), respectively. For the other groups of compounds, they are approximately equal to the formal valences and ionization energies of the metals: $\text{Log } K_S \approx -(2.303nRT)^{-1}(0.99\Delta H^{\circ}_{T,L} - I_e)$.

Reversible intercalation of ammonia molecules into a layered double hydroxide structure without exchanging nitrate counter-ions

Gregorio Guadalupe Carbajal Arizaga, Fernando Wypych, Felipe Castillón Barraza and Oscar Edel Contreras Lopez

Page 2324

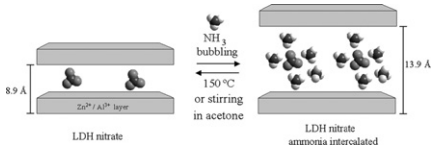

LDH-nitrate precipitated with ammonia expands the interlayer space if ammonia is bubbled up to pH 10. The basal distance decreased when the compound was heated at 150 °C or stirred in acetone. Nitrate ions are not exchanged.

Crystal structure and physical properties of quaternary clathrates $Ba_8Zn_xGe_{46-x-y}Si_y$, $Ba_8(Zn,Cu)_xGe_{46-x}$ and $Ba_8(Zn,Pd)_xGe_{46-x}$

Navida Nasir, Andriy Grytsiv, Nataliya Melnychenko-Koblyuk, Peter Rogl, Ingeborg Bednar and Ernst Bauer

Page 2329

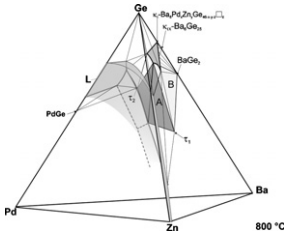

Quaternary phase diagram of Ba–Pd–Zn–Ge system at 800 °C.

New ternary rare-earth metal boride carbides $R_{15}B_4C_{14}$ (R = Y, Gd–Lu) containing BC_2 units: Crystal and electronic structures, magnetic properties

Volodymyr Babizhetskyy, Arndt Simon, Hansjürgen Mattausch, Kurt Hiebl and Chong Zheng

Page 2343

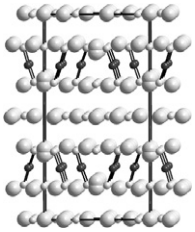

The ternary rare earth boride carbides $R_{15}B_4C_{14}$ (R = Y, Gd–Lu) were prepared from the elements by arc-melting followed by annealing in silica tubes at 1270 K for 1 month. $Tb_{15}B_4C_{14}$ is a new member of the rare-earth metal boride carbide series in which the finite quasi-molecular CBC entities as well as isolated C atoms are embedded in the voids of the metal atom matrix. The structure of $Tb_{15}B_4C_{14}$ contains two types of slabs: one slab contains finite bent CBC units and isolated carbon atoms whereas another is formed only from octahedral coordinated single carbon atoms. The electronic structure for the idealized composition corresponds to an electron partitioning according to $(Tb^{3+})_{15}(C^{4-})_6(CBC^{5-})_4 \bullet e^-$ giving rise to a single electron per formula for Tb–Tb framework bonding. The magnetism of the ternary rare earth boride carbides $R_{15}B_4C_{14}$ (R = Tb, Dy, Er) is characterized by the onset of ferromagnetic order below $T < 150$ K.

Synthesis, crystal structure and thermal behavior of $Sr_3B_2SiO_8$ borosilicate

M.G. Krzhizhanovskaya, R.S. Bubnova, S.V. Krivovichev, O.L. Belousova and S.K. Filatov

Page 2352

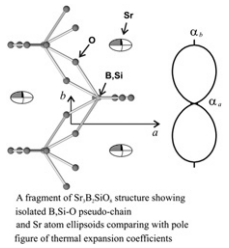

A fragment of $Sr_3B_2SiO_8$ structure showing isolated B,Si–O pseudo-chain and Sr atom ellipsoids, comparing with pole figure of thermal expansion coefficients.

Cetyltrimethylammonium bromide assisted self-assembly of $NiTe_2$ nanoflakes: Nanoflake arrays and their photoluminescence properties

Ling Jiang, Ying-Jie Zhu and Jing-Biao Cui

Page 2358

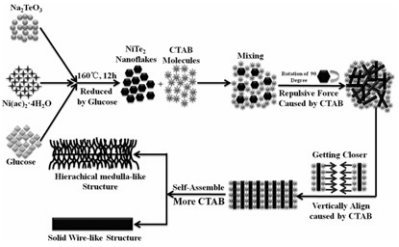

$NiTe_2$ nanoflakes and their self-assembled nanoflake arrays have been prepared by a single-step hydrothermal method using $Ni(CH_3COO)_2 \cdot 4H_2O$, Na_2TeO_3, glucose, and cetyltrimethylammonium bromide (CTAB).

Thermoluminescence and synchrotron radiation studies on the persistent luminescence of $BaAl_2O_4:Eu^{2+},Dy^{3+}$

L.C.V. Rodrigues, R. Stefani, H.F. Brito, M.C.F.C. Felinto, J. Hölsä, M. Lastusaari, T. Laamanen and M. Malkamäki

Page 2365

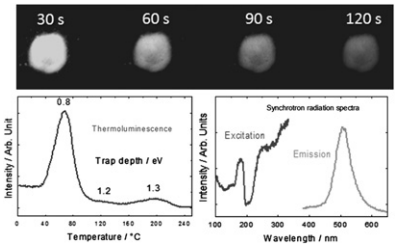

$BaAl_2O_4:Eu^{2+},Dy^{3+}$ phosphors: Thermoluminescence glow curve and synchrotron radiation spectra. Persistent luminescence photographs obtained after ceased UV irradiation.

Continued

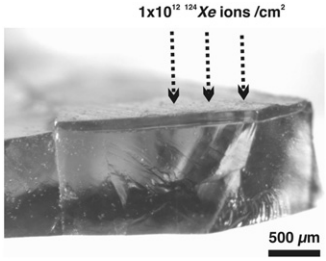

Cordierite single-crystal specimen showing the color change from pale blue (unirradiated) to a yellowish brown layer (irradiated) after exposure to relativistic ^{124}Xe ions at a fluence of 1×10^{12} ions per cm^2.

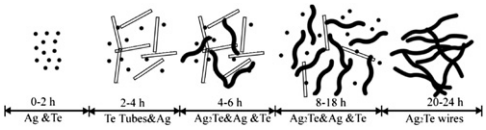

Ultra-long single crystal β-Ag_2Te nanowires with the diameter of about 300 nm were fabricated by the solvothermal route in ethylene glycol (EG) system without any template. The diagram displays the variation of the phases and morphologies of products with different reaction time.

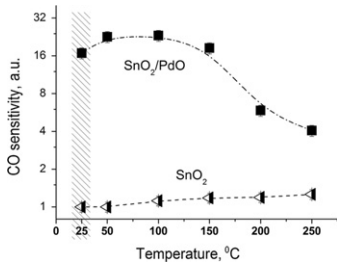

Nanocrystalline SnO_2 modified by PdO/Pd clusters exhibit high CO sensitivity at room temperature. An extensive study revealed surface OH-groups participation in CO oxidation on SnO_2 leading to enhanced sensitivity at low operating temperature (25–150 °C). PdO/Pd clusters supposedly initiate a chain of CO reactions with surface hydroxyls.

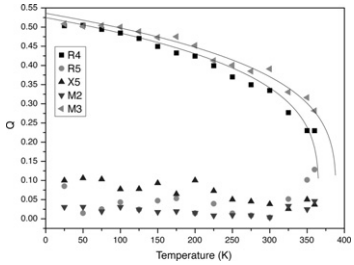

Variable temperature powder neutron diffraction measurements reveal that $Sr_{0.92}NbO3$ undergoes a sequence of phase transitions $Pnma \rightarrow P4/mbm \rightarrow Pm3m$ with unanticipated softening of the *M* point rather than *R* point resulting in the formation of the primitive tetragonal intermediate.

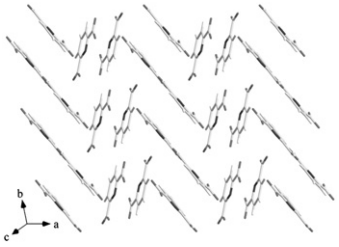

Wire representation exhibiting 2,6-pyridinedicarboxylate groups that are packed parallel.

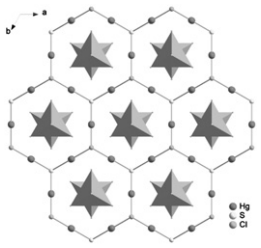

Two novel compounds were synthesized via solid-state reactions. One is the first example of ternary zinc–Q–X chalcogenides and the other is the first example of quaternary IIB–Q–X metal chalcogenides.

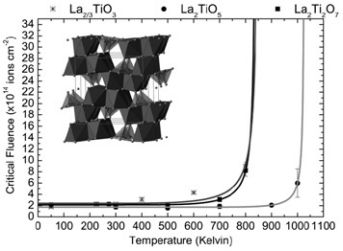

La_2TiO_5 with atypical co-ordination for Ti, TiO_5 is found to be different in radiation resistance to $La_2Ti_2O_7$ and $La_{2/3}TiO_3$. Irradiation of La–Ti–O, and La–Al–O based systems has found that radiation damage resistance is related to the ability of the system to disorder.

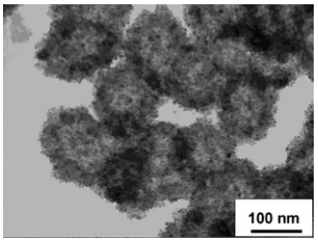

A new one-step solvothermal method was developed to prepare Pd nanoparticles embedded hierarchically porous TiO_2 hollow spheres. Due to its unique nanostructure, the prepared TiO_2/Pd modified GC electrode exhibit a high sensitivity (226.72 μA mM^{-1} cm^{-2}), a relatively low reduction potential (−0.2 V), a fast response time (<3 s) and a relatively low detection limit of 3.81 μM ($S/N=3$) towards H_2O_2.

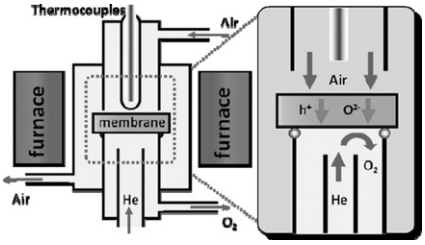

Partially Cu-substituted $BaFe_{1-y}Cu_yO_{3-\delta}$ ($y=0.1$–0.15) membranes exhibit high oxygen permeation fluxes at intermediate high temperatures (700–930 °C) under an air/He gradient, due to the stabilization of the cubic perovskite phase by the substitution.

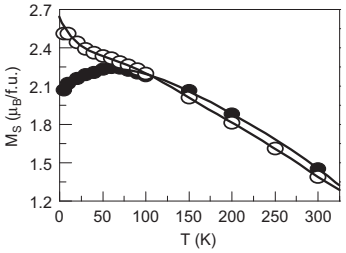

Temperature dependence of saturation magnetization of $(Sr_{1.8}Eu_{0.2})FeMoO_6$ (filled circle) and $(Sr_{1.8}Nd_{0.2})FeMoO_6$ (open circle).

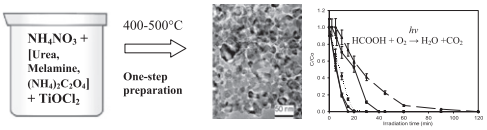

Ammonium nitrate melts stabilized by nitrogen-containing organic molecules can be applied for expedite one-step preparation of highly dispersed oxides, as exemplified by synthesis of titania photocatalysts.

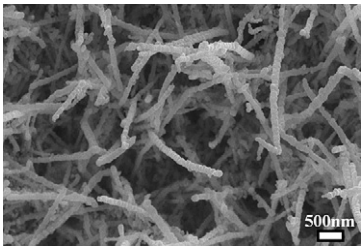

Novel GaN/Mn_3O_4 core–shell nanowires were synthesized and the effects of thermal annealing on the structure, photoluminescence, and magnetic properties were investigated.

Continued

Micro-Raman analysis of titanium oxide/carbon nanotubes-based nanocomposites for hydrogen sensing applications
S. Santangelo, G. Messina, G. Faggio, A. Donato, L. De Luca, N. Donato, A. Bonavita and G. Neri
Page 2451

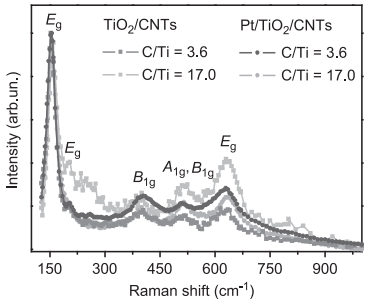

Micro-Raman analysis of TiO_2/CNTs and Pt/TiO_2/CNTs hybrids for H_2 sensing applications evidences that regardless of C/Ti molar ratio titania crystallizes in the anatase phase. The very small size of TiO_2 crystallites (4.3–5.0 nm) is responsible for the observed phonon confinement effects.

Microstructure and electrical–optical properties of cesium tungsten oxides synthesized by solvothermal reaction followed by ammonia annealing
Jing-Xiao Liu, Yoshihiko Ando, Xiao-Li Dong, Fei Shi, Shu Yin, Kenji Adachi, Takeshi Chonan, Akikazu Tanaka and Tsugio Sato
Page 2456

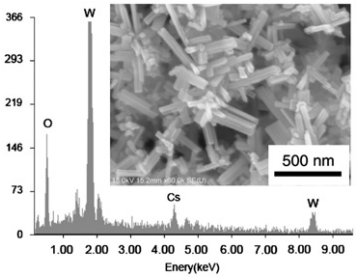

Cesium tungsten oxides (Cs_xWO_3) with different morphology were synthesized by solvothermal reaction, and the effects of post-ammonia annealing on the microstructure and electrical–optical properties were investigated.

The anti-perovskite type hydride $InPd_3H_{0.89}$
H. Kohlmann, A.V. Skripov, A.V. Soloninin and T.J. Udovic
Page 2461

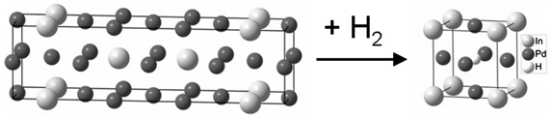

Hydrogen induces a rearrangement in $InPd_3$ from a $ZrAl_3$ type structure to a cubic $AuCu_3$ type structure, thus forming an anti-perovskite type hydride $InPd_3H_{0.89}$

Microwave hydrothermal synthesis and photocatalytic activity of $AgIn_5S_8$ for the degradation of dye
Wenjuan Zhang, Danzhen Li, Meng Sun, Yu Shao, Zhixin Chen, Guangcan Xiao and Xianzhi Fu
Page 2466

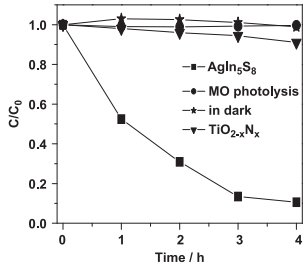

Compared with $TiO_{2-x}N_x$, $AgIn_5S_8$ has exhibited a superior activity under the same condition.

Synthesis, structure, solid-state thermolysis, and thermodynamic properties of new heterometallic complex $Li_2Co_2(Piv)_6(NEt_3)_2$
Zn.V. Dobrohotova, A.A. Sidorov, M.A. Kiskin, G.G. Aleksandrov, K.S. Gavrichev, A.V. Tyurin, A.L. Emelina, M.A. Bykov, A.S. Bogomyakov, I.P. Malkerova, A.S. Alihanian, V.M. Novotortsev and I.L. Eremenko
Page 2475

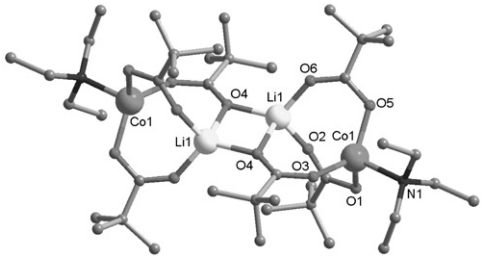

The solid-state thermolysis, study of the vaporization process, and temperature dependence of C_p for the new heterometallic complex $Co_2Li_2(Piv)_6(NEt_3)_2$ were performed. Decomposition of $Co_2Li_2(Piv)_6(NEt_3)_2$ results in the formation of $LiCoO_2$.

Structural characterization of the $FeTiO_3$–$MnTiO_3$ solid solution
Xiang Wu, Shan Qin and Leonid Dubrovinsky
Page 2483

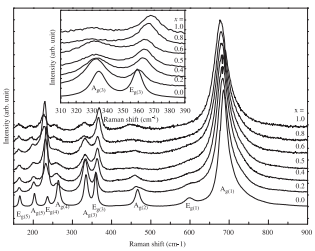

Raman spectra of the $(Mn_{1-x}Fe_x)TiO_3$ $(0.0 \le x \le 1.0)$ system. Inset: the enlarged view from 310 to 390 cm^{-1}. $E_{g(3)}$ shifts to high frequency and the remaining shifts to low frequency as $x$$FeTiO_3$ content increases.

One-step fabrication and characterization of silica-sheathed ITO nanowires

Hyoun Woo Kim, Hyo Sung Kim, Han Gil Na, Ju Chan Yang, Rino Choi, Jae Kyeong Jeong, Chongmu Lee and Doo Young Kim

Page 2490

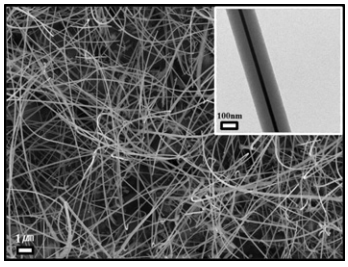

Novel ITO/amorphous SiO_x core–shell structures were synthesized by thermal evaporation. A Au-catalyzed VLS process is the dominant mechanism for the ITO nanowires, whereas SiO_x was grown in a tubular structure.

Rapid Communications

A new $BaB_2Si_2O_8$:Eu^{2+}/Eu^{3+}, Tb^{3+} phosphor – Synthesis and photoluminescence properties

M.P. Saradhi, S. Boudin, U.V. Varadaraju and B. Raveau

Page 2496

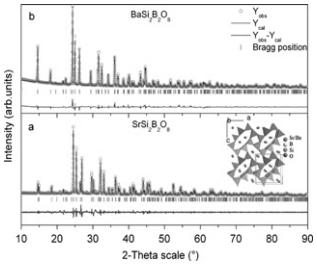

The figure shows structure refinement of both $MB_2Si_2O_8$ [M = Sr, Ba]. The structure refinement of newly synthesized phase $BaB_2Si_2O_8$ was carried out by taking $SrB_2Si_2O_8$ as starting structure model. Inset in the figure shows the structure projection of $BaB_2Si_2O_8$. The Sr^{2+}/Ba^{2+} are embedded in polyanionic network formed by corner sharing BO_4^{5-} and SiO_4^{4-} tetrahedral that intern form interconnected layers of 4 and 8 membered rings perpendicular to b-axis.

Transport properties, specific heat and thermal conductivity of GaN nanocrystalline ceramic

Czesław Sułkowski, Andrzej Chuchmała, Andrzej J. Zaleski, Marcin Matusiak, Jan Mucha, Paweł Głuchowski and Wiesław Stręk

Page 2501

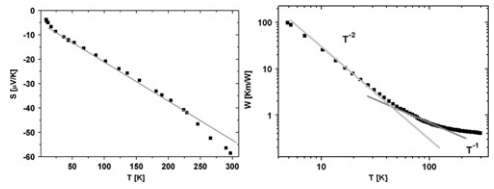

Thermal resistivity and thermopower measurements indicates the high phonon scattering and lack of phonon-drag contribution to thermopower in GaN nanoceramics pressed under 4 GPa at 800 °C.

Geometric parameterization of the $YBaCo_4O_7$ structure type: Implications for stability of the hexagonal form and oxygen uptake

M. Avdeev, V.V. Kharton and E.V. Tsipis

Page 2506

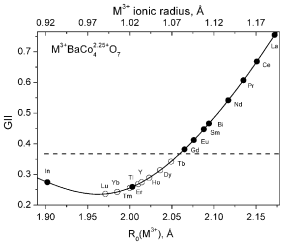

Global Instability Index (GII) for an $M^{3+}BaCo_4^{2.25+}O_7$.